Analytical modeling of transient temperature in powder feed metal additive manufacturing during heating and cooling stages

Jinqiang Ning[1] · Daniel E. Sievers[2] · Hamid Garmestani[3] · Steven Y. Liang[1]

Abstract

This work presents a physics-based predictive model for transient temperature during heating state and cooling state in powder feed metal additive manufacturing (PFMAM). The deposition dimension, heat transfer boundary conditions, laser absorption, and latent heat are considered in the presented model. The temperature solution is constructed from the superposition of moving point heat source solution and heat sink solution based on a stationary coordinate with respect to the part boundary. The heat source solution is activated during heating state and deactivated during cooling state. The temperature profiles and molten pool evolution were predicted with respect to the processing time in single-track deposition of PFMAM of Inconel 718. Close-agreements were observed upon validation to the experimental results in the literature. The presented model has high computational efficiency without resorting to the mesh and iterative calculation. The high prediction accuracy and high computational efficiency allow the temperature prediction for large-scale parts, and process-parameter planning through inverse analysis.

1 Introduction

Metal additive manufacturing (MAM) has been extensively studied in the past because of its capability of producing geometrically complex parts with effective cost [1, 2]. Powder feed metal additive manufacturing (PFMAM) combines laser cladding with rapid prototype process to build the geometrically complex component from metal powders in a layer-by-layer manner. Defects such as crack, delamination [3], balling effect [4], undesired mechanical properties [5, 6], and part distortion [7] are frequently observed in the PFMAM due to the repeatedly rapid heat and solidification, which lead to high temperature levels and large temperature gradients. Therefore, the understanding of the thermal mechanism and the temperature prediction in PFMAM are needed. Different approaches have been developed for the temperature analysis in MAM. They can be broadly classified into three categories: experimental approach, finite element analysis (FEA)-based numerical modeling, and physics-based analytical modeling.

In situ temperature measurement is difficult and inconvenient in manufacturing processes due to the elevated temperatures and restricted accessibility [8, 9]. Contact technique and non-contact technique were employed for temperature measurements in MAM. Contact techniques such as thermocouples can only measure the temperatures at far field such as on or inside substrate [10], despite the fact that the temperatures inside build has a direct influence on the quality and thus the functionality of the produced parts. Non-contact techniques such as infrared (IR) pyrometer and thermal imaging camera can only measure the temperatures on the exposed surfaces [11, 12]. More information on in situ measurement techniques in MAM can be found in the review literature [13–15]. Moreover, the post-process measurement based on the solidified microstructure was also employed for temperature analysis, which needs extensive experimental works for sample preparation including cutting, polishing, etching, etc., [16].

✉ Jinqiang Ning
  jinqiangning@gatech.edu

✉ Steven Y. Liang
  steven.liang@me.gatech.edu

1   George W. Woodruff School of Mechanical Engineering, Georgia Institute of Technology, 801 Ferst Drive, Atlanta, GA 30332-0405, USA

2   The Boeing Company, 499 Boeing Boulevard, Huntsville, AL 35824, USA

3   School of Materials Science and Engineering, Georgia Institute of Technology, 771 Ferst Drive NW, Atlanta, GA 30332, USA

To address the difficulty and inconvenience in experimental measurements, FEA-based numerical models were developed to predict different MAM processes. Roberts et al. developed a numerical model to predict the three-dimensional temperature distribution in selective laser melting (SLM) using element birth and death technique, in which a heat source with Gaussian distributed profile was employed [17]. Patil et al. developed a numerical model to predict the temperature distribution in selective laser sintering (SLS), which employed a heat source with different shape of Gaussian distribution [18]. Fu et al. predicted the temperature distribution in SLM with a numerical model using solid bulk material properties and powder material properties, respectively [19]. Improved prediction accuracy was reported using powder material properties upon validation to the experimental measurement of molten pool dimensions. Dai et al. developed a numerical model considering volume shrinkage during the cooling state of SLM [20]. Labudovic et al. predicted the temperature distribution in directed metal deposition (DMD) with a numerical model [21]. Criales et al. investigated the sensitivity of material and process parameters in the prediction of SLM [22]. Zhang et al. investigated the influence of substrate preheating in the prediction of DMD [23]. Recent numerical models have considered the influence of molten pool dynamics and powder packing on the temperature prediction [24–26]. Residual stress and part distortion were also investigated through numerical modeling [27, 28]. A detailed discussion of numerical models is out of the scope of this work. More information can be found in the review literature [29–31]. Although numerical models have made considerable progress in predicting different MAM processes, the high computational cost due to mesh and iteration is still the major drawback, which prevents the prediction for large-scale parts and process-parameter planning through inverse analysis.

Physics-based analytical models have been reported with significantly higher computational efficiency than numerical models because of the avoidance of mesh and iteration [32, 33]. Analytical models were developed to predict the MAM processes. Van Elsen et al. summarized three moving heat source solutions, namely point moving heat source solution, semi-ellipsoidal moving heat source solution and uniform moving heat source solution [34]. The following assumptions were made in those solutions: semi-infinite medium; isotropic and homogeneous material; and steady-state condition. A moving coordinate with an origin at moving laser location was used in the temperature prediction, which neglected the influence of part dimension. The moving heat source solutions were originally developed by Carslaw and Jaeger [35]. Ning et al. further developed the original point moving heat source to predict the in-process temperatures in SLM for a dimensional part with a stationary coordinate considering laser power absorption, latent heat, scanning

strategy, and powder packing [36]. Huang et al. and Fathi et al. further developed the original point moving heat source solution for temperature prediction of multi-layer printing using superposition of multiple real and virtual point heat sources, in which Green's function was used to consider part dimension [37, 38]. Cline et al. proposed a heat source solution assuming the heat source intensity follows Gaussian distribution [39]. This solution becomes the point moving heat source solution by reducing the beam radius to zero. Pinkerton et al. predicted temperature distribution and molten pool dimension in DMD using a line moving heat source solution [40, 41]. The line moving heat source solution was originally developed by Rosenthal for temperature prediction in welding an infinite-thin plate [42]. The line moving heat source solution was further developed with the transformation from the moving coordinate to the stationary (absolute) coordinate using two image heat sources [43]. Li et al. further developed the line heat source solution for temperature prediction of multi-layer printing using superposition of multiple point heat sources with positive and negative power for the past heat sources and adiabatic boundary condition [44]. However, the heat transfer boundary conditions specifically the heat loss from convection and radiation at the part boundary, has not been considered in the developed models. To address the neglection of heat transfer boundary conditions, semi-analytical models were developed for temperature prediction. Cline's solution was further developed to consider the heat loss from the molten pool with iterative calculations based on mass and energy balance [45]. Peyre et al. developed a semi-analytical model to predict temperatures in DMD, in which an analytical model and a numerical model were employed to the deposition geometry and temperature distribution, respectively [46]. Yang et al. developed another semi-analytical model to predict the temperatures in SLM, in which an analytical model and a numerical model were employed to characterize the moving heat source and impose heat transfer boundary conditions [47]. However, the involvement of iteration-based numerical model unavoidably compromises computational efficiency.

Nowadays, the heat transfer boundary conditions are been calculated without the involvement of FEA or iteration-based numerical calculations, which reduce the computational efficiency, and thus reduce the usefulness in the prediction of large-scale part, and process parameters planning through inverse analysis.

This work presents an analytical model to predict the transient temperature during heating and cooling state PFMAM, in which the heat loss is calculated using heat sink solution without resorting to any FEA or iteration-based calculations. A stationary (absolute) coordinate with an origin at part boundary was employed in the temperature prediction. The temperature solution was constructed from the superposition of a point moving heat source solution and multiple

stationary heat sink solutions considering the non-uniform temperature and non-uniform heat loss at the part boundary. In addition, the laser power absorption was considered as a power coefficient; the latent heat was considered using the heat integration method. The presented model was tested through temperature predictions in single-track scans in PFMAM of Inconel 718. An experimental validation is included.

2 Methodology

This work presents an analytical model to predict the transient temperature in PFMAM during heating state and cooling state. The heating state and cooling state are distinguished by the fact whether the continuous heat input from laser power exists. They are distinguished by the time when laser scan completes in the model. The temperature rise due to heat input from the laser heat source is calculated using the point moving heat source solution. The temperature drop due to the heat loss from convection and radiation at the part boundary is calculated using the heat sink solutions. The heat source is activated during heating state and deactivated during cooling state. A stationary (absolute) coordinate is employed for the temperature prediction as illustrated in Fig. 1, where the red arrow, green arrows, and blue arrows represent the heat input, the heat loss from convection and radiation to the ambiance, the heat loss from conduction to the substrate, respectively. The following assumptions are
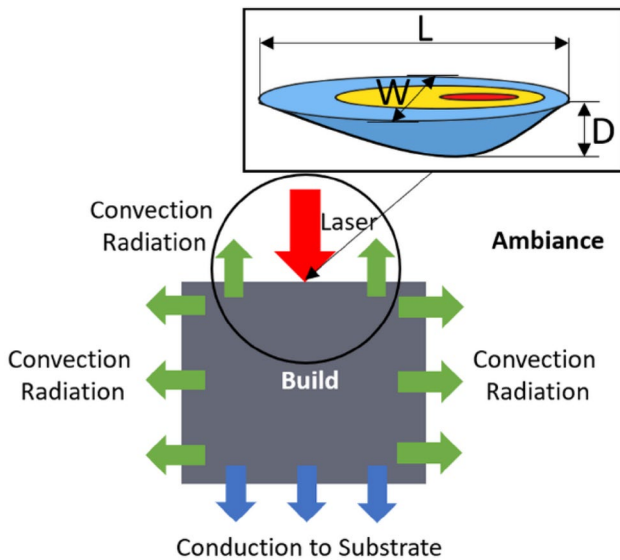

Fig. 1 Schematic drawing of thermal mechanism in PFMAM. Red, green and blue arrows represent the heat input for laser, the heat loss from convection, and radiation to the ambiance, and the heat loss from conduction to substrate, respectively. L, W, D denote the molten pool length, width, and depth

enforced in this study: (1) the workpiece and substrate are made of the same material; (2) the material is isotropic and homogeneous; (3) the material properties are temperature-independent; (4) the laser heat source is a point moving heat source. For comparison, other analytical models were developed based on the semi-infinite medium assumption, as illustrated in the black circle in Fig. 1, which neglect the heat loss form part boundaries and thus compromise the prediction accuracy.

The temperature solution is constructed from the superposition of the active/inactive point moving heat source solution and heat sink solutions as the following.

$$\theta(X, Y, Z, t) = \theta_L - \theta_S$$
(heating state at $0 < t < L/V$)

$$\theta(X, Y, Z, t) = \theta\left(X, Y, Z, t_L\right) - \theta_S$$
(cooling state at $t > L/V$), \hfill (1)

where θ_L is the temperature rise due to heat input for the laser source; θ_S is the temperature drop due to the heat loss from heat sinks on the part boundaries; X, Y, Z are the coordinate; $t, t_L = L/V$ are the current time and the laser scan time respectively, L is scan length, V is scan velocity.

The heat balance equation can be expressed as the following:

$$\frac{\partial \rho u}{\partial t} + \frac{\partial \rho H V}{\partial x} = \nabla \cdot (k \nabla T) + \dot{q}, \hfill (2)$$

where u is internal energy, H is enthalpy, ρ is density, k is conductivity, and $\dot{q}$ is a volumetric heat source, t is time, x is the distance from the heat source, V is heat source moving velocity along the x-direction, and T is temperature.

The heat conduction equation was derived from the heat balance equation with $V = 0$, and $du = cdT$ as the following.

$$\frac{\partial^2 T}{\partial x^2} + \frac{\partial^2 T}{\partial y^2} + \frac{\partial^2 T}{\partial z^2} = \frac{1}{\kappa} \frac{\partial T}{\partial t} + \dot{q}, \hfill (3)$$

where κ is thermal diffusivity ($\kappa = k/\rho c$, where k, ρ, c are thermal conductivity, density, and specific heat, respectively), x, y, z are the distances from the heat source.

The moving point heat source solution was derived from the heat conduction equation as originally proposed by Carslaw and Jaeger [35]. Considering the laser power absorption (η), the heat source solution becomes

$$\theta_L(x, y, z, t) = \frac{P\eta}{8\rho C_p (\pi \kappa)^{\frac{3}{2}}} \int_0^t \frac{\exp\left[-\frac{(x-V(t-t'))^2 + y^2 + z^2}{4\kappa(t-t')}\right]}{(t-t')^{\frac{3}{2}}} dt'$$
\hfill (4)

The temperature solution is rewritten by integrating t' from 0 to t as

$$\theta_L(x, y, z, t) = \frac{P\eta}{2Rk_t\pi^{\frac{3}{2}}} \exp\left(\frac{Vx}{2\kappa}\right) \int_{\frac{R}{2\sqrt{\kappa t}}}^{\infty} \exp\left[-\xi^2 - \left(\frac{V^2R^2}{16\kappa^2\xi^2}\right)\right]d\xi,$$

$$(5)$$

where $R^2 = x^2 + y^2 + z^2$, t is the current time, t' is previous time, x, y, z are the corresponding distances from the laser source, ξ is a time-related integration variable. The substrate material is assumed to the same as the build. The heat conduction mechanism inside the substrate and the build are thus the same. The heat conduction from laser power to the build and substrate is considered by the above temperature solution.

Considering the temperature distribution and non-uniform heat loss from convection and radiation at the part boundary, the part boundary is mathematically discretized into multiple sections (multiple heat sinks). The heat sink solution is derived from the heat source solution with an equivalent power for heat loss and zero moving velocity because the heat sink is a portion of the stationary part boundary. The heat sink temperature is estimated using the point moving heat source solution at the center of each heat sink.

$$Q_{\text{conv}} = Ah(T - T_0) \tag{6}$$

$$Q_{\text{rad}} = A\varepsilon\sigma(T^4 - T_0^4), \tag{7}$$

where Q_{conv} and Q_{rad} denote heat loss due to convection and radiation, respectively, A is the area of heat sink, h is convection coefficient, ε is emissivity, σ is Stefan–Boltzmann constant, T is the temperature of heat sink, T_0 is room temperature. The number of heat sinks and the area of each heat sink are negatively correlated on a given boundary area. The number of heat sinks can be empirically determined or determined based on calibration. However, the more heat sinks the more computationally expensive of the model because of the summation of each heat sink effect. In addition, the heat sink solution is derived from the point heat source solution which has singularity issue at the heat source location. Therefore, a tiny heat sink area is more susceptible to the inherent singularity issue, which reduces the prediction accuracy.

$$\theta_S(x, y, z, t, n) = \sum_{i=1}^{n} \left[h(T_i - T_0) + \varepsilon\sigma(T_i^4 - T_0^4)\right] \cdot$$
$$\frac{A_i}{2Rk\pi^{\frac{3}{2}}} \int_{\frac{R}{2\sqrt{\kappa t}}}^{\infty} \exp(-\xi^2)d\xi \tag{8}$$

The final temperature solution then becomes:

$$\theta_t(X, Y, Z, t) = \theta_L(x, y, z, t) - \theta_S(x, y, z, t, n)$$
$$\text{(heating state at } 0 < t < L/V)$$

Table 1 Material properties of Inconel 718 [48, 50]

Name	Symbol	Value	Unit
Density	ρ	8820	kg/m³
Thermal conductivity	k	11	W/(m K)
Specific heat	c	420	J/(kg K)
Latent heat	H_f	210,000	J/Kg
Room temperature	T_0	25	°C
Solidus temperature	T_s	1260	°C
Liquidus temperature	T_l	1533	°C
Heat convection coefficient	h	25	W/(m² K)
Emissivity	ε	0.8	1
Stefan–Boltzmann constant	σ	5.67×10^{-8}	W/(m² K⁴)

$$\theta_t(X, Y, Z, t) = \theta_L(X, Y, Z, t_L) - \theta_S(x, y, z, t, n),$$
$$\text{(cooling state at } t > L/V) \tag{9}$$

where n is the number of heat sinks, $t, t_L = L/V$ are the current time and the laser scan time respectively, L is scan length, V is scan velocity.

Latent heat is considered in the presented model using the heat integration method, which lowers the molten pool temperature during the heating state and increases the molten pool temperature during the cooling state by the following amount due to the phase transformation [34].

$$\Delta T = L_f/c \tag{10}$$

where L_f is the latent heat, c is the specific heat.

3 Results and discussion

In this work, the transient temperatures in PFMAM of Inconel 718 were predicted using the presented model. The temperature profiles and molten pool evolution were predicted with respect to process time in single-track scans during heating state and cooling state. The predicted temperatures were validated to the experimental measurement from the literature [48], in which a K-type thermocouple was attached to the substrate to record the temperature history. The PFMAM system combines a YC50 cladding head and 2 kW Ytterbium doped, continuous wave, fiber laser operating at a wavelength of 1070 nm. The Inconel 718 powder was produced from gas atomization with size ranging from 15 to 45 μm. The laser absorption was adopted as 0.3. The laser absorption is affected by the laser setting and powder characterization such as laser wavelength, powder material properties, powder packing-related surface roughness, laser-workpiece stand-off distance, and thus the adopted laser absorption should be valid only in this study [49]. The

Table 2 Process condition and part dimension [48]

| Name	Symbol	Value	Unit
Power	P	1800	W
Absorption	η	0.3	1
Scan velocity	V	400	mm/min
Part 1 length	L_1	5	mm
Part 1 width	W_1	5	mm
Part 1 height	D_1	2	mm
Part 2 length	L_2	110	mm
Part 2 width	W_2	1.48	mm
Part 2 height	D_2	1.27	mm

Fig. 2 Schematic drawing of heat loss from convection and radiation from the boundary of a dimensional part. The green arrows represent heat loss from each heat sink. The heat sink on the back sides and bottom are not shown

material properties of Inconel 718 were adopted as solid bulk material properties at room temperature as given in Table 1.

The process condition was given as in Table 2. Two different parts, part 1 and part 2, were used for temperature predictions. Part 1 was used to investigate the relationship between laser scanning location with respect to the part boundary and the significance of heat transfer boundary conditions. Part 2 was used to investigate molten pool evolution including molten pool growth and stabilization during heating state and the molten pool shrinkage during cooling state. The predicted temperatures in part 2 were validated to the experimental temperatures in the literature.

Temperature predictions in multiple single-track scans on part 1 were predicted using the presented model for bounded medium and using the original point moving heat source model for semi-infinite medium separately. A stationary (absolute) coordinate with an origin at the part boundary was employed in the prediction. For temperature calculation considering bounded medium, the part boundary was mathematically discretized into many sections to calculate the heat loss from convection and radiation at the part boundary as illustrated in Fig. 2. For temperature calculation considering semi-infinite medium, the heat loss from the part boundary was neglected.

To investigate the relationship between laser scanning location and the influence of heat transfer boundary condition, the temperature profiles were predicted in multiple single-track scans at different locations on part 1 considering bounded medium and semi-infinite medium as illustrated in Fig. 3, where the solid lines represented the predicted temperature profiles considering heat loss for the bounded medium; the dashed line represented the predicted temperature profiles neglecting the heat loss for semi-infinite medium. The red stars denote the center of each heat sink, where the heat sink temperatures were estimated using the point heat source solutions. The number of heat sinks on part 1 was empirically determined as 1/mm^2. Temperature profiles were plotted as top views at five different laser
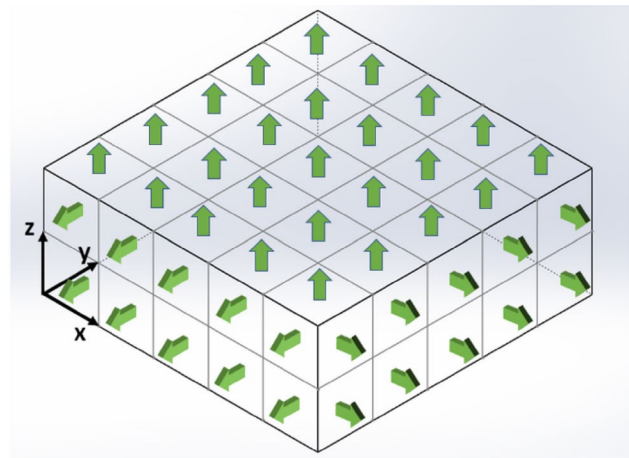
locations, specifically (a) $x=4$ mm $y=0.5$ mm (b) $x=4$ mm $y=1.5$ mm (c) $x=4$ mm $y=2.5$ mm (d) $x=4$ mm $y=3.5$ mm (e) $x=4$ mm $y=4.5$ mm. A significant discrepancy was observed between predictions considering heat loss and predictions neglecting heat loss. The closer the scan location to the part boundary ($y=0$ mm and $y=5$ mm), the greater the discrepancy of the temperature profile and thus the greater the influence of heat loss, and vice versa. The average computational time for temperature prediction at each location was recorded as 71.88 s with an increment of 20 μm in x, y, z directions.

In addition, the molten pool length and depth were calculated by comparing to the material melting temperature. A symmetric pattern was observed for molten pool dimensions at symmetric scan locations as illustrated in Fig. 4.

The temperature evolution was predicted in a single-track scan on part 2 during heating state and cooling state of PFMAM as illustrated in Fig. 5. The mass addition was considered as pre-existing part in a rectangular shape at room temperature. The heat loss on two boundaries on the y–z planes at $x=0$ mm and $x=115$ mm was neglected because of the relatively smaller areas.

Inconel 718 powder was deposited along y-direction from 0 to 115 mm (corresponding time from 0 to 17.25 s) with laser heating path from 0 to 110 mm (corresponding time from 0 to 16.5 s). The molten pool width was assumed to the same as the part width for such a thin wall structure. The 2D temperature profiles during PBMAM was plotted as in Fig. 6, where (a–h) were corresponding to 0.001 s, 0.01 s, 0.1 s, 1 s, 10 s, 16.5 s, 21.5 s, 31.5 s, respectively. Each calculated region has a size of 4 mm in length and 1.27 mm in height with an increment of 20 μm in both directions. Four heat sinks ($A=1$ mm$\times 1.27$ mm) were empirically
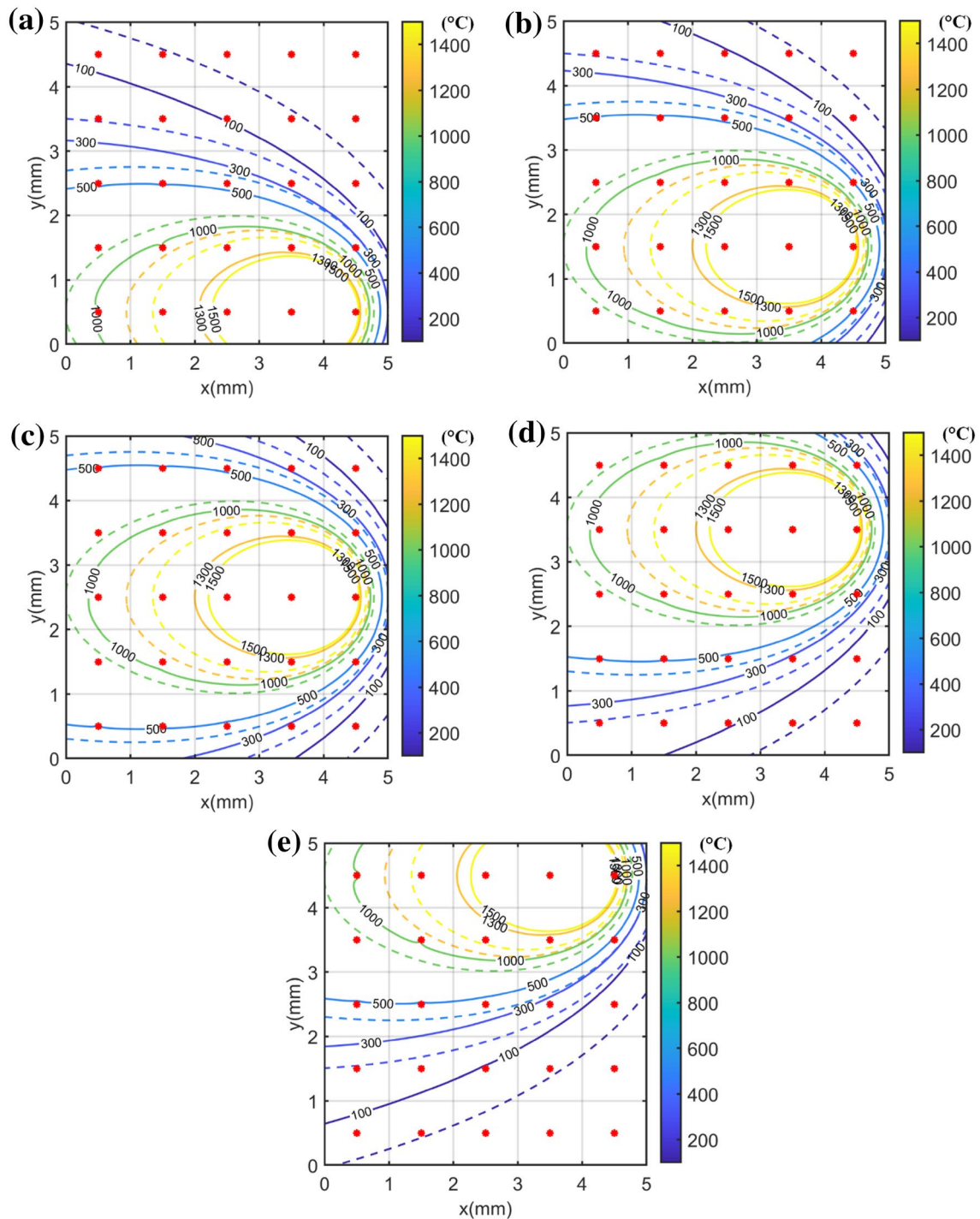
Fig. 3 Predicted temperatures with various laser scanning location in the *y*-direction (**a**) y = 0.5 mm (**b**) y = 1.5 mm (**c**) y = 2.5 mm (**d**) y = 3.5 mm (**e**) y = 4.5 mm. The temperature unit is °C. Solid lines denote predicted temperatures for bounded medium; dash lines denote predicted temperature for semi-infinite medium. Red stars denote the heat sink center where the temperatures are estimated using the moving point heat source solution

determined on the top boundary (*x*–*y* plane at $z = 1.27$), font and back boundaries (*x*–*z* planes at $z = -0.74$ mm and 0.74 mm).

The molten pool evolution was calculated by comparing the predicted temperature profiles to the material melting temperature. The molten pool growth and stabilization during heating state and shrinkage during cooling state are
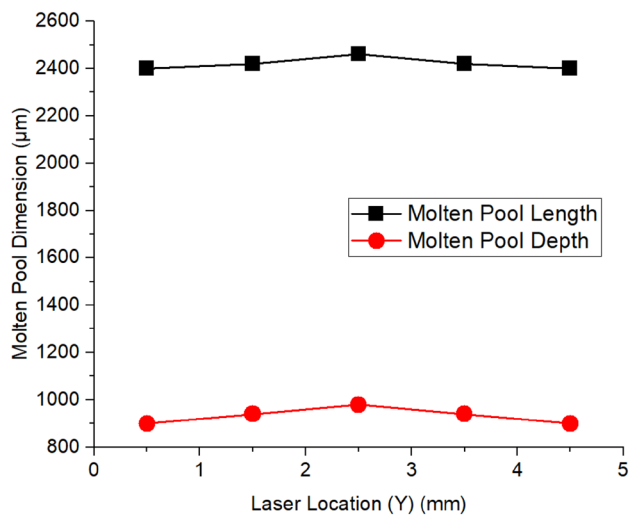
Fig. 4 Predicted molten pool dimensions considering bounded medium with various laser scan location ($x = 4$ mm, $y = 0.5$, 1.5, 2.5, 3.5, 4.5 mm)
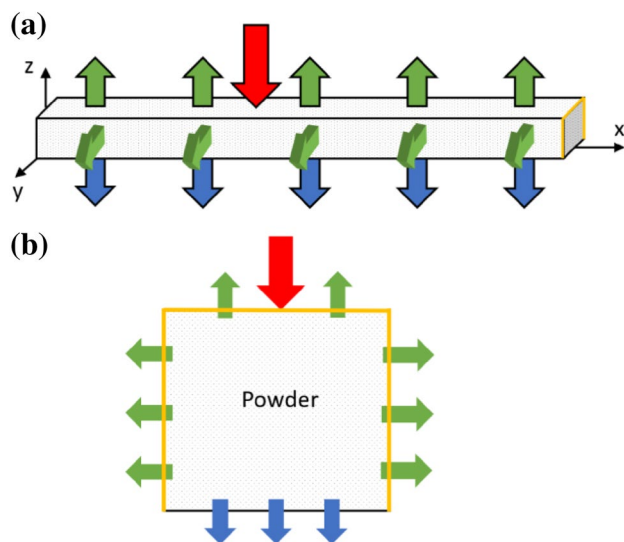

Fig. 5 Schematic drawing of heat transfer condition in single-track powder feed metal additive manufacturing. **a** Isometric view **b** cross-sectional view on y–z plane. Red, green and blue arrows represent heat input for laser, heat loss from convection and radiation to ambiance environment, heat loss from conduction to the substrate

illustrated in Figs. 7 and 8, respectively. Molten pool stabilized at its maximum size after 1 s. Molten pool shrank starting at 16.5 s and diminished after 215 s. The molten pool dimensions after 60 s during the cooling state were predicted with regression analysis using polynomial function based on the predicted molten pool dimensions from 16.5 and 100 s to resolve the singularity issue in point moving heat source solution; specifically the temperature at heat source location mathematically becomes infinite as in Eq. (5). The

polynomial function was selected from trial and error based on the performance of curve fitting on the predicted values during the cooling state. The average computational time of temperature prediction at each time during heat state and cooling state was recorded as 80 s and 144 s, respectively, with x increment and z increment of 20 µm. For comparison, FEA models require at least half hour for temperature prediction with comparable prediction accuracy depending on the part size and mesh resolution [19, 21].

The predicted temperatures at location $x = 55$ mm, $y = 3$ mm, $z = 0$ mm during heating state and cooling state were validated to the experimental measurements from thermocouple at the same location in the coordinate illustrated in Fig. 5. The heat loss from the top boundary of the substrate was neglected due to the small distance from the measurement location to the build, and relatively lower temperature. Close-agreements were observed between the predicted temperatures and the experimental measurement as illustrated in Fig. 9. The temperature drop before the cooling state was observed because of increasing distance from the moving laser to the thermocouple location. The temperature drop during cooling sate was observed because of the heat loss from convection and radiation. The experimental peak temperature and predicted peak temperature during the heating state were 521.2 °C and 495.6 °C, respectively, as illustrated in Fig. 9a. The prediction error on peak temperature was 4.91%. The slight mismatch between prediction and measurement might be caused by the employed point moving heat source, which neglected the influence of the laser beam profile [51–53]. The laser beam profile should be considered as future works to further improve the prediction accuracy. In addition, the temperature-independent materials properties, and the simplified rectangular-shaped workpiece, and the chosen number of heat sinks might also affect the deviation between prediction and experimental measurement.

With the benefits of high prediction accuracy and high computational efficiency, the presented model can be used for temperature prediction in the real application for the large-scale part and process-parameter planning through inverse analysis [54, 55]. Improvements can be made to further increase the prediction accuracy and usefulness of the analytical thermal model. The heat source intensity distribution, the realistic geometry of deposited powders, the heat accumulation in multi-track scanning, and multi-layer scanning should be considered as future works.

4 Conclusion

This work presents a physics-based analytical model to predict the transient temperature and molten pool evolution during heating state and cooling sate in single-track scans of PFMAM with consideration of part dimension,
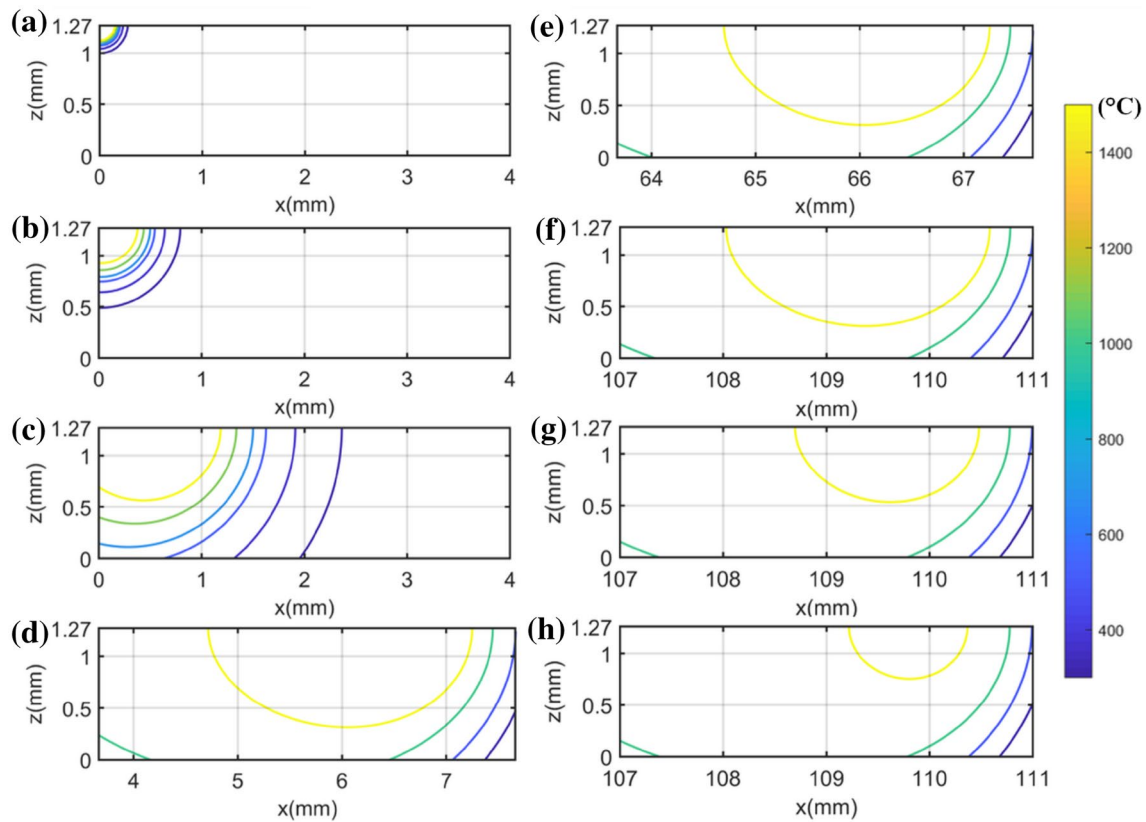
Fig. 6 Predicted temperature evolution during heat state and cooling state of PFMAM for part 2 at **a** 0.001 s **b** 0.01 s **c** 0.1 s **d** 1 s **e** 10 s **f** 16.5 s **g** 21.5 s **h** 31.5 s. The temperature unit is °C. Cooling state starts from 16.5 s
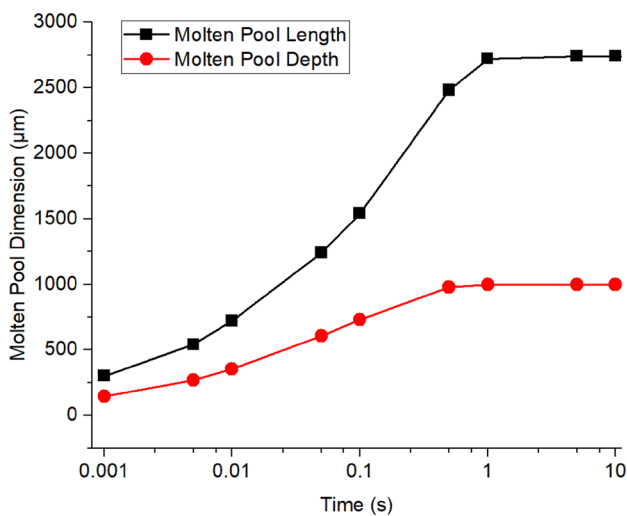

Fig. 7 Predicted molten pool growth and stabilization during heating state of PFMAM in the single-track scan for part 2. A logarithmic scale was used for the horizontal axis for a clear presentation of motel pool growth and stabilization
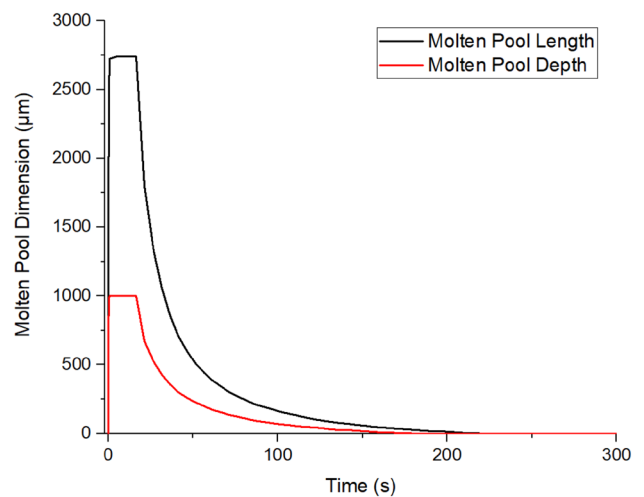

Fig. 8 Predicted molten pool evolution during heating state and cooling state of PFMAM in the single-track scan for part 2

heat transfer boundary conditions, laser absorption, and latent heat. The temperature solution is constructed from the superposition of heat source solution and heat sink

solution. The heat source solution is activated during the heating state and deactivated during the cooling state. The presented model has promising short computational time without resorting to FEA or any iteration-based calculations.
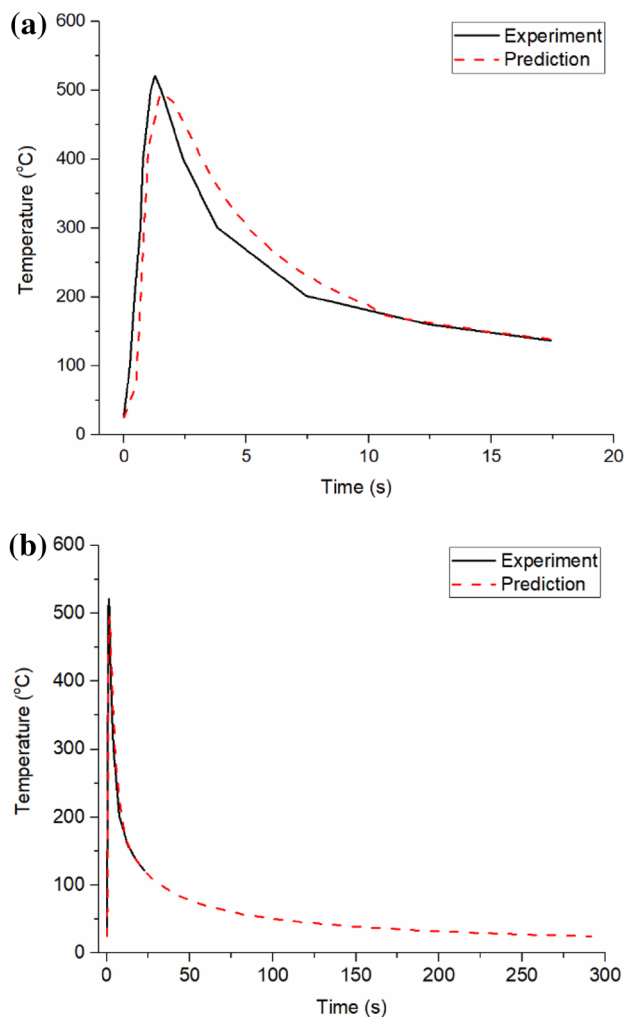
(a)

(b)

Fig. 9 Validation of temperatures to the experimental measurements using a K-type thermocouple placed on the substrate ($x=55$ mm $y=3$ mm $z=0$ mm). **a** Temperature validation during heating state of PFMAM; **b** temperature validation during heating state and cooling state of PFMAM. Red dash lines denote predicted temperature. Black solid lines denote experimental temperature in the literature [48]

To test the presented model, temperature profiles in single-track scans at different locations during PFMAM of Inconel 718 were predicted. A positive relationship between laser distance to the part boundary and the significance of heat loss was observed. Then the temperature profiles during heating state and cooling state in a single-track scan were predicted. Molten pool evolution was investigated with the predicted temperature profiles. Close agreement was observed between predicted temperatures and experimental measurement. In addition, expected high computational efficiency was observed from the recorded computational time for each temperature prediction. With the benefits of high prediction accuracy and high computational efficiency, the presented model can

be used for temperature investigation in PFMAM for the large-scale parts and process-parameter planning through inverse analysis.

References

1. D.S. Thomas, S.W. Gilbert, Costs and cost effectiveness of additive manufacturing. NIST Spec. Publ. **1176**, 12 (2014). https://doi.org/10.6028/NIST.SP.1176
2. I. Gibson, D.W. Rosen, B. Stucker, *Additive Manufacturing Technologies*, vol. 17 (Springer, New York, 2014)
3. H. Gong, K. Rafi, H. Gu, T. Starr, B. Stucker, Analysis of defect generation in Ti–6Al–4 V parts made using powder bed fusion additive manufacturing processes. Addit. Manuf. **1**, 87–98 (2014). https://doi.org/10.1016/j.addma.2014.08.002
4. J.P. Kruth, G. Levy, F. Klocke, T.H.C. Childs, Consolidation phenomena in laser and powder-bed based layered manufacturing. CIRP Ann. **56**(2), 730–759 (2007). https://doi.org/10.1016/j.cirp.2007.10.004
5. Z. Wang, E. Denlinger, P. Michaleris, A.D. Stoica, D. Ma, A.M. Beese, Residual stress mapping in Inconel 625 fabricated through additive manufacturing: method for neutron diffraction measurements to validate thermomechanical model predictions. Mater. Des. **113**, 169–177 (2017). https://doi.org/10.1016/j.matdes.2016.10.003
6. A.J. Sterling, B. Torries, N. Shamsaei, S.M. Thompson, D.W. Seely, Fatigue behavior and failure mechanisms of direct laser deposited Ti–6Al–4V. Mater. Sci. Eng. A **655**, 100–112 (2016). https://doi.org/10.1016/j.msea.2015.12.026
7. J.C. Heigel, P. Michaleris, T.A. Palmer, In situ monitoring and characterization of distortion during laser cladding of Inconel® 625. J. Mater. Process. Technol. **220**, 135–145 (2015). https://doi.org/10.1016/j.jmatprotec.2014.12.029
8. J. Ning, S. Liang, Prediction of temperature distribution in orthogonal machining based on the mechanics of the cutting process using a constitutive model. J. Manuf. Mater. Process. **2**(2), 37 (2018). https://doi.org/10.3390/jmmp2020037
9. J. Ning, S.Y. Liang, Predictive modeling of machining temperatures with force-temperature correlation using cutting mechanics and constitutive relation. Materials **12**(2), 284 (2019). https://doi.org/10.3390/ma12020284
10. J.C. Heigel, M.F. Gouge, P. Michaleris, T.A. Palmer, Selection of powder or wire feedstock material for the laser cladding of Inconel® 625. J. Mater. Process. Technol. **231**, 357–365 (2016). https://doi.org/10.1016/j.jmatprotec.2016.01.004
11. A.J. Pinkerton, M. Karadge, W.U.H. Syed, L. Li, Thermal and microstructural aspects of the laser direct metal deposition of waspaloy. J. Laser Appl. **18**(3), 216–226 (2006). https://doi.org/10.2351/1.2227018
12. D.A. Kriczky, J. Irwin, E.W. Reutzel, P. Michaleris, A.R. Nassar, J. Craig, 3D spatial reconstruction of thermal characteristics in directed energy deposition through optical thermal imaging. J. Mater. Process. Technol. **221**, 172–186 (2015). https://doi.org/10.1016/j.jmatprotec.2015.02.021
13. S.K. Everton, M. Hirsch, P. Stravroulakis, R.K. Leach, A.T. Clare, Review of in situ process monitoring and in situ metrology for metal additive manufacturing. Mater. Des. **95**, 431–445 (2016). https://doi.org/10.1016/j.matdes.2016.01.099

14. G. Tapia, A. Elwany, A review on process monitoring and control in metal-based additive manufacturing. J. Manuf. Sci. Eng. **136**(6), 060801 (2014). https://doi.org/10.1115/1.4028540

15. S. Clijsters, T. Craeghs, S. Buls, K. Kempen, J.P. Kruth, In situ quality control of the selective laser melting process using a high-speed, real-time melt pool monitoring system. Int. J. Adv. Manuf. Technol. **75**(5–8), 1089–1101 (2014). https://doi.org/10.1007/s00170-014-6214-8

16. L.E. Criales, Y.M. Arısoy, B. Lane, S. Moylan, A. Donmez, T. Özel, Laser powder bed fusion of nickel alloy 625: experimental investigations of effects of process parameters on melt pool size and shape with spatter analysis. Int. J. Mach. Tool Manuf. **121**, 22–36 (2017). https://doi.org/10.1016/j.ijmachtools.2017.03.004

17. I.A. Roberts, C.J. Wang, R. Esterlein, M. Stanford, D.J. Mynors, A three-dimensional finite element analysis of the temperature field during laser melting of metal powders in additive layer manufacturing. Int. J. Mach. Tool Manuf. **49**(12–13), 916–923 (2009). https://doi.org/10.1016/j.ijmachtools.2009.07.004

18. R.B. Patil, V. Yadava, Finite element analysis of temperature distribution in single metallic powder layer during metal laser sintering. Int. J. Mach. Tool Manuf. **47**(7–8), 1069–1080 (2007)

19. C.H. Fu, Y.B. Guo, Three-dimensional temperature gradient mechanism in selective laser melting of Ti-6Al-4V. J. Manuf. Sci. Eng. **136**(6), 061004 (2014). https://doi.org/10.1115/1.4028539

20. K. Dai, L. Shaw, Finite element analysis of the effect of volume shrinkage during laser densification. Acta Mater. **53**(18), 4743–4754 (2005). https://doi.org/10.1016/j.actamat.2005.06.014

21. M. Labudovic, D. Hu, R. Kovacevic, A three dimensional model for direct laser metal powder deposition and rapid prototyping. J. Mater. Sci. **38**(1), 35–49 (2003). https://doi.org/10.1023/A:1021153513925

22. L.E. Criales, Y.M. Arısoy, T. Özel, Sensitivity analysis of material and process parameters in finite element modeling of selective laser melting of Inconel 625. Int. J. Adv. Manuf. Technol. **86**(9–12), 2653–2666 (2016). https://doi.org/10.1007/s00170-015-8329-y

23. K. Zhang, S. Wang, W. Liu, R. Long, Effects of substrate preheating on the thin-wall part built by laser metal deposition shaping. Appl. Surf. Sci. **317**, 839–855 (2014). https://doi.org/10.1016/j.apsusc.2014.08.113

24. M. Xia, D. Gu, G. Yu, D. Dai, H. Chen, Q. Shi, Porosity evolution and its thermodynamic mechanism of randomly packed powder-bed during selective laser melting of Inconel 718 alloy. Int. J. Mach. Tool Manuf. **116**, 96–106 (2017). https://doi.org/10.1016/j.ijmachtools.2017.01.005

25. P. Wei, Z. Wei, Z. Chen, Y. He, J. Du, Thermal behavior in single track during selective laser melting of AlSi10Mg powder. Appl. Phys. A **123**(9), 604 (2017). https://doi.org/10.1007/s00339-017-1194-9

26. Y. Xiang, S. Zhang, Z. Wei, J. Li, P. Wei, Z. Chen, L. Jiang, Forming and defect analysis for single track scanning in selective laser melting of Ti6Al4V. Appl. Phys. A **124**(10), 685 (2018). https://doi.org/10.1007/s00339-018-2056-9

27. G. Vastola, G. Zhang, Q.X. Pei, Y.W. Zhang, Controlling of residual stress in additive manufacturing of Ti6Al4V by finite element modeling. Addit. Manuf. **12**, 231–239 (2016). https://doi.org/10.1016/j.addma.2016.05.010

28. S. Afazov, W.A. Denmark, B.L. Toralles, A. Holloway, A. Yaghi, Distortion prediction and compensation in selective laser melting. Addit. Manuf. **17**, 15–22 (2017). https://doi.org/10.1016/j.addma.2017.07.005

29. B. Schoinochoritis, D. Chantzis, K. Salonitis, Simulation of metallic powder bed additive manufacturing processes with the finite element method: a critical review. Proc. Inst. Mech. Eng. Part B J. Eng. Manuf. **231**(1), 96–117 (2017). https://doi.org/10.1177/0954405414567522

30. A.J. Pinkerton, Advances in the modeling of laser direct metal deposition. J. Laser Appl. **27**(S1), S15001 (2015). https://doi.org/10.2351/1.4815992

31. J.L. Bartlett, X. Li, An overview of residual stresses in metal powder bed fusion. Addit. Manuf. **27**, 131–149 (2019). https://doi.org/10.1016/j.addma.2019.02.020. **(In Press)**

32. J. Ning, S.Y. Liang, A comparative study of analytical thermal models to predict the orthogonal cutting temperature of AISI 1045 steel. Int. J. Adv. Manuf. Technol. **102**, 1–11 (2019). https://doi.org/10.1007/s00170-019-03415-9

33. J. Ning, V. Nguyen, S.Y. Liang, Analytical modeling of machining forces of ultra-fine-grained titanium. Int. J. Adv. Manuf. Technol. **101**, 1–10 (2018). https://doi.org/10.1007/s00170-018-2889-6

34. M. Van Elsen, M. Baelmans, P. Mercelis, J.P. Kruth, Solutions for modelling moving heat sources in a semi-infinite medium and applications to laser material processing. Int. J. Heat Mass Transf. **50**(23–24), 4872–4882 (2007). https://doi.org/10.1016/j.ijheatmasstransfer.2007.02.044

35. H. Carslaw, J. Jaeger, *Conduction of Heat in Solids* (Oxford Science Publication, Oxford, 1990)

36. J. Ning, D.E. Sievers, H. Garmestani, S.Y. Liang, Analytical modeling of in-process temperature in powder bed additive manufacturing considering laser power absorption, latent heat, scanning strategy, and powder packing. Materials **12**(5), 808 (2019). https://doi.org/10.3390/ma12050808

37. Y. Huang, M.B. Khamesee, E. Toyserkani, A new physics-based model for laser directed energy deposition (powder-fed additive manufacturing): from single-track to multi-track and multi-layer. Opt. Laser Technol. **109**, 584–599 (2019). https://doi.org/10.1016/j.optlastec.2018.08.015

38. A. Fathi, E. Toyserkani, A. Khajepour, M. Durali, Prediction of melt pool depth and dilution in laser powder deposition. J. Phys. D Appl. Phys. **39**(12), 2613 (2006). https://doi.org/10.1088/0022-3727/39/12/022

39. H.E. Cline, T. Anthony, Heat treating and melting material with a scanning laser or electron beam. J. Appl. Phys. **48**(9), 3895–3900 (1977). https://doi.org/10.1063/1.324261

40. A.J. Pinkerton, L. Li, Modelling the geometry of a moving laser melt pool and deposition track via energy and mass balances. J. Phys. D Appl. Phys. **37**(14), 1885 (2004). https://doi.org/10.1088/0022-3727/37/14/003

41. A.J. Pinkerton, L. Li, The significance of deposition point standoff variations in multiple-layer coaxial laser cladding (coaxial cladding standoff effects). Int. J. Mach. Tool Manuf. **44**(6), 573–584 (2004). https://doi.org/10.1016/j.ijmachtools.2004.01.001

42. D. Rosenthal, The theory of moving sources of heat and its application of metal treatments. Trans. ASME **68**, 849–866 (1946)

43. H. Tan, J. Chen, F. Zhang, X. Lin, W. Huang, Process analysis for laser solid forming of thin-wall structure. Int. J. Mach. Tool Manuf. **50**(1), 1–8 (2010). https://doi.org/10.1016/j.ijmachtools.2009.10.003

44. J. Li, Q. Wang, P.P. Michaleris, An analytical computation of temperature field evolved in directed energy deposition. J. Manuf. Sci. Eng. **140**(10), 101004 (2018). https://doi.org/10.1115/1.4040621

45. M.N. Ahsan, A.J. Pinkerton, An analytical–numerical model of laser direct metal deposition track and microstructure formation. Modell. Simul. Mater. Sci. Eng. **19**(5), 055003 (2011). https://doi.org/10.1088/0965-0393/19/5/055003

46. P. Peyre, P. Aubry, R. Fabbro, R. Neveu, A. Longuet, Analytical and numerical modelling of the direct metal deposition laser process. J. Phys. D Appl. Phys. **41**(2), 025403 (2008). https://doi.org/10.1088/0022-3727/41/2/025403

47. Y. Yang, M.F. Knol, F. van Keulen, C. Ayas, A semi-analytical thermal modelling approach for selective laser melting. Addit. Manuf. **21**, 284–297 (2018). https://doi.org/10.1016/j.addma.2018.03.002

48. T.R. Walker, C.J. Bennett, T.L. Lee, A.T. Clare, A validated analytical-numerical modelling strategy to predict residual stresses in single-track laser deposited IN718. Int. J. Mech. Sci. **151**, 609–621 (2019). https://doi.org/10.1016/j.ijmecsci.2018.12.004

49. C.D. Boley, S.A. Khairallah, A.M. Rubenchik, Calculation of laser absorption by metal powders in additive manufacturing. Appl. Opt. **54**(9), 2477–2482 (2015). https://doi.org/10.1364/AO.54.002477

50. A.A. Deshpande, D.W.J. Tanner, W. Sun, T.H. Hyde, G. McCartney, Combined butt joint welding and post weld heat treatment simulation using SYSWELD and ABAQUS. Proc. Inst. Mech. Eng. Part L J. Mater. Des. Appl. **225**(1), 1–10 (2011). https://doi.org/10.1177/14644207JMDA349

51. H. Qi, J. Mazumder, L. Green, G. Herrit, Laser beam analysis in direct metal deposition process. J Laser Appl. **17**(3), 136–143 (2005). https://doi.org/10.2351/1.1896965

52. T.T. Roehling, S.S. Wu, S.A. Khairallah, J.D. Roehling, S.S. Soezeri, M.F. Crumb, M.J. Matthews, Modulating laser intensity profile ellipticity for microstructural control during metal additive manufacturing. Acta Mater. **128**, 197–206 (2017). https://doi.org/10.1016/j.actamat.2017.02.025

53. M. Rasch, C. Roider, S. Kohl, J. Strauß, N. Maurer, K.Y. Nagulin, M. Schmidt, Shaped laser beam profiles for heat conduction welding of aluminium-copper alloys. Opt. Lasers Eng. **115**, 179–189 (2019). https://doi.org/10.1016/j.optlaseng.2018.11.025

54. J. Ning, S.Y. Liang, Model-driven determination of Johnson-Cook material constants using temperature and force measurements. Int. J. Adv. Manuf. Technol. **97**(1–4), 1053–1060 (2018). https://doi.org/10.1007/s00170-018-2022-x

55. J. Ning, V. Nguyen, Y. Huang, K.T. Hartwig, S.Y. Liang, Inverse determination of Johnson-Cook model constants of ultra-fine-grained titanium based on chip formation model and iterative gradient search. Int. J. Adv. Manuf. Technol. **99**(5–8), 1131–1140 (2018). https://doi.org/10.1007/s00170-018-2508-6